Dirac nodal lines and flat-band surface state in the functional oxide RuO_2

Vedran Jovic,[1,2] Roland J. Koch,[1] Swarup K. Panda,[3] Helmuth Berger,[4] Philippe Bugnon,[4] Arnaud Magrez,[4] Kevin E. Smith,[2,5] Silke Biermann,[3,6] Chris Jozwiak,[1] Aaron Bostwick,[1] Eli Rotenberg,[1] and Simon Moser[1,7,*]

[1]*Advanced Light Source, E. O. Lawrence Berkeley National Laboratory, Berkeley, California 94720, USA*

[2]*School of Chemical Sciences and Centre for Green Chemical Sciences, The University of Auckland, Auckland 1142, New Zealand*

[3]*Centre de Physique Théorique, Ecole Polytechnique, CNRS-UMR7644, Université Paris-Saclay, 91128 Palaiseau, France*

[4]*Institute of Physics, Ecole Polytechnique Fédérale de Lausanne (EPFL), CH-1015 Lausanne, Switzerland*

[5]*Department of Physics, Boston University, Boston, Massachusetts 02215, USA*

[6]*Collège de France, 11 place Marcelin Berthelot, 75005 Paris, France*

[7]*Physikalisches Institut, Universität Würzburg, D-97074 Würzburg, Germany*

The efficiency and stability of RuO_2 in electrocatalysis has made this material a subject of intense fundamental and industrial interest. The surface functionality is rooted in its electronic and magnetic properties, determined by a complex interplay of lattice-, spin-rotational, and time-reversal symmetries, as well as the competition between Coulomb and kinetic energies. This interplay was predicted to produce a network of Dirac nodal lines (DNLs), where the valence and conduction bands touch along continuous lines in momentum space. Here we uncover direct evidence for three DNLs in RuO_2 by angle-resolved photoemission spectroscopy. These DNLs give rise to a flat-band surface state that is readily tuned by the electrostatic environment, and that presents an intriguing platform for exotic correlation phenomena. Our findings support high spin-Hall conductivities and bulk magnetism in RuO_2, and are likely related to its catalytic properties.

Introduction. Ruthenium dioxide is a functional semimetal of wide industrial use, in part stemming from its remarkable electronic/ionic conduction properties and favorable thermal and chemical stability [1]. RuO_2 is corrosion resistant and its diffusion properties are beneficial for pH and dissolved oxygen sensing electrodes, as e.g., employed in water quality monitoring sensors [2]. Further, due to particularly high Coulombic efficiencies and good mass transport properties, nanoporous RuO_2 is a prototype conversion material in metal oxide lithium-ion battery electrodes [3] with high charge storage capacity (supercapacitors) [4].

The interest in RuO_2 stems also from its efficiency in electrocatalytic processes [5], especially in the electrochemical reduction of CO_2 to methanol [6] and in the industrial recycling of chlorine from HCl (Deacon process) [7]. The RuO_2 (110) surface, in particular, is among the highest performing anodes for the oxygen evolution reaction in photoelectrochemical water splitting and electrolysis [8]. Such qualities can be related to specific properties of the Fermi surface: First-principle calculations based on density functional theory (DFT) claim magnetic moments on the RuO_2 surface to be responsible for low overpotentials in the evolution reaction of ground-state magnetic (triplet) oxygen from nonmagnetic water, resulting in high catalytic efficiencies [9]. Such local magnetic moments are confirmed by neutron-scattering experiments, and attributed to a spin density wave instability driven by a particularly large density of states at nested "hot spots" in the Fermi surface [10]. These in turn are believed to be the direct consequence of the nonsymmorphic symmetry of the rutile RuO_2 crystal structure [11,12], establishing an intimate link between the fundamental properties and the surface functionality.

Dirac nodal lines in RuO_2. The significance of nonsymmorphicity in RuO_2 was recently discussed within the framework of topology and relativistic Dirac physics [13]. Symmetry considerations in conjunction with DFT predicted a network of two types of Dirac nodal lines (DNLs) [14–23], where the valence and conduction bands touch close to the Fermi level along continuous lines in momentum space: (A) First, time-reversal and inversion symmetry in unison with a mirror symmetry protect a band crossing within the (110) and $(\bar{1}10)$ planes. This produces a network of fourfold degenerate ($2\times$ spin and $2\times$ orbital) and topologically nontrivial DNLs (DNL1) [13], outlined by blue lines in the Brillouin zone (BZ) of Fig. 1(a). (B) The second type of DNL in RuO_2 is topologically trivial and protected by a nonsymmorphic glide mirror symmetry [13]. In brief, the RuO_2 lattice is a bipartite composition of two sublattices with different RuO_6 octahedral orientation that are related by a fractional lattice translation of half a body diagonal and a reflection about the (100) plane. The consequent band folding gives rise to two sets of bands, producing—in conjunction with time-reversal symmetry—fourfold degenerate DNL2s along the $k_x = \pi/a$ and $k_y = \pi/a$ boundary planes of the primitive BZ [22,24]. In the presence of spin-orbit coupling (SOC) the DNL1s are gapped, which was predicted to result in high spin-Hall conductivities [13], similar as in IrO_2 [25]. The DNL2s, however, remain strictly symmetry protected along the XM and MA lines in the BZ [green lines in Fig. 1(a)] [13,26].

*simon.moser@physik.uni-wuerzburg.de

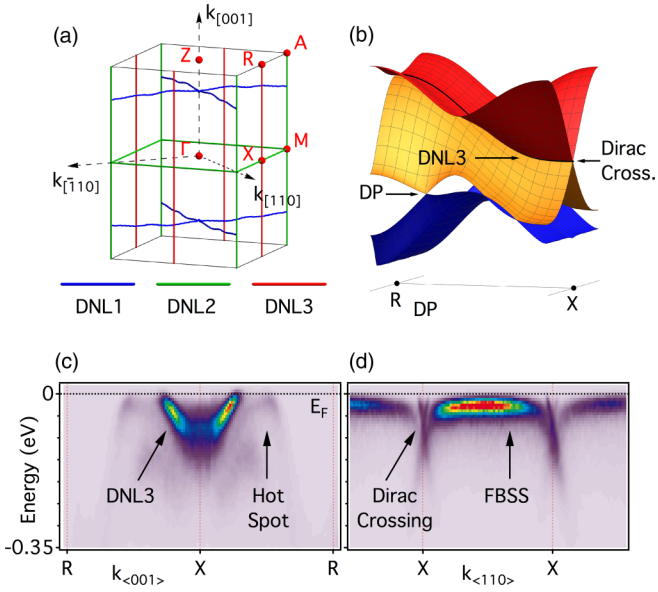

FIG. 1. Dirac nodal lines (DNLs) in RuO_2. (a) Brillouin zone of RuO_2, summarizing the calculated k-space trajectories of the three DNLs. (b) DFT band-structure model of RuO_2, showing the fourfold band crossing of DNL3 along XR, and a Dirac point at DP. (c) ARPES map along XR outlining DNL3 and the "hot spot" states. (d) Perpendicular ARPES map, showing the Dirac crossing that forms DNL3, as well as the FBSS.

This scenario is confirmed by our state-of-the-art ARPES experiments on the (110) surface of slightly n-type, Ir-doped RuO_2 (see Supplemental Material S4 [27] as well as Refs. [28,29]), and presents a rare observation of relativistic Dirac fermions in a functional oxide of genuine industrial use. Even more fascinating, we find evidence for an additional, unexpected DNL3 of type (B) along XR, producing a continuous Dirac crossing at the Fermi level (Fig. 1), and remaining surprisingly intact despite considerable SOC. This DNL3 serves as an anchor line for a nondispersive FBSS [Fig. 1(d)], the analog of the theoretically predicted drumhead surface state [14,19,30]. Its diverging density of states can give rise to novel exotic phenomena such as surface superconductivity [31], long-range Coulomb interaction [32], or graphenelike Landau levels [33], and is likely involved in surface catalytic processes. Finally, we reveal the nested hot spot features in the Fermi surface [Fig. 1(c)] that are held responsible for the spin density wave scenario of magnetism in RuO_2 [10], and a postulated pillar of its catalytic efficiency [9].

ARPES in the XR plane. Our comprehensive ARPES results in Fig. 2 substantiate these claims. Panel (a) shows a Fermi surface taken with $h\nu = 69$ eV photon energy and probes the RuO_2 BZ along a (110) plane containing the X and the R high-symmetry points [see Fig. 2(c) and Supplemental Material S3 [27]). We observe four main spectral contributions, marked in panel (a) and summarized in the schematics of panel (b). (I) First, and most importantly, we observe double arc structures centered at the X points. These represent the two branches of the Dirac crossing that forms DNL3. The arcs extend toward the zone center, and form a faint onion dome. (II) Second, we find intense spectral features labeled DP. These are the intersection points of DNL1 with the XR momentum plane, as outlined in panel (c). (III) Third, intense "hot streaks" mark the projections of DNL1 onto the XR plane. Their intersection with the XR BZ boundary line marks the hot spot features in the Fermi surface, claimed responsible for the magnetic instability in RuO_2 [10]. (IV) Last, we identify two prominent arcs spanning in between adjacent DNL3s, the signature of the FBSS.

(I) Let us first discuss the unexpected DNL3 along XR: Figure 2(d) shows horizontal band structure cuts for five selected momenta $k_{\langle 001\rangle}$ [outlined in (b)], revealing the evolution of the Dirac crossing from X towards R. From $k_{\langle 001\rangle} = 0$ (d_1) to ~ 0.25 Å^{-1} (d_5), the crossing point moves toward lower binding energies (black arrows), and eventually passes the Fermi level at $k_{\langle 001\rangle} \sim 0.28$ Å^{-1}. Our DFT calculation in panel (e) [34–36] reproduces the Dirac crossing in d_1 astonishingly well, but locates it 0.56 eV above the experimental value of ~ -0.1 eV, a striking deficit of our simplified DFT approach. The corresponding three-dimensional band-structure model of Fig. 1(b) correctly produces the continuous fourfold band crossing of DNL3 along XR. The degeneracy, however, is supposed to be lifted by SOC as seen in Fig. 2(f). As the degeneracy is strictly symmetry protected along the XM line [13], the SOC-induced splitting effect is weak in the vicinity of the X point and remains unresolved by our ARPES experiment.

(II) The features labeled DP in Fig. 2(a) represent the intersection points of DNL1 with the (110) momentum plane, highlighted in panel (c). Both ARPES and DFT reveal the corresponding Dirac crossing in panel (g), but the SOC-induced gap remains again unresolved. Similar as with DNL3, theory locates the crossing point about 0.15 eV above the experimental value of -10 meV.

(III) Figure 2(h) shows ARPES cuts along $k_{\langle 001\rangle}$, taken at representative momenta $k_{\langle 110\rangle}$ as outlined in (b). Next to the features forming the onion dome, we observe the continuous evolution of the Dirac states at DP in (h_1) toward a band with a holelike parabolic band maximum at the hot spots in h_5, as correctly predicted by DFT [blue in panel (i)]. This evolution is smooth and responsible for the intense hot streaks in the Fermi surface of Fig. 2(a), the projection of DNL1 onto the XR momentum plane [see panel (c) and Supplemental Material S4 [27]]. The nesting of these parallel hot streaks along commensurate nesting vectors, as well as their simultaneous electron- and holelike character, favors potential Fermi surface instabilities such as spin- or charge-density waves. In addition, the intersections of these hot streaks with the XR BZ boundary lines, i.e., the hot spots, are symmetry protected by the nonsymmorphic glide plane of RuO_2. The fourfold degeneracy of these bands is thus lifted only by SOC [panel (i)] and/or by a magnetic spin-density wave instability—the claimed origin of magnetic moments in RuO_2 [10].

(IV) Last, we return to Fig. 2(d) and note that these panels also trace the energy dispersion of the FBSS along $k_{\langle 110\rangle}$, as well as its anchoring in the Dirac crossing. Its photon energy independence (see Supplemental Material S4 [27]), as well as the fact that the bulk DFT description in panel (e) misses this state, clearly demonstrates its surface character. Far away from X, the FBSS remains nondispersively flat at ~ -30 meV,

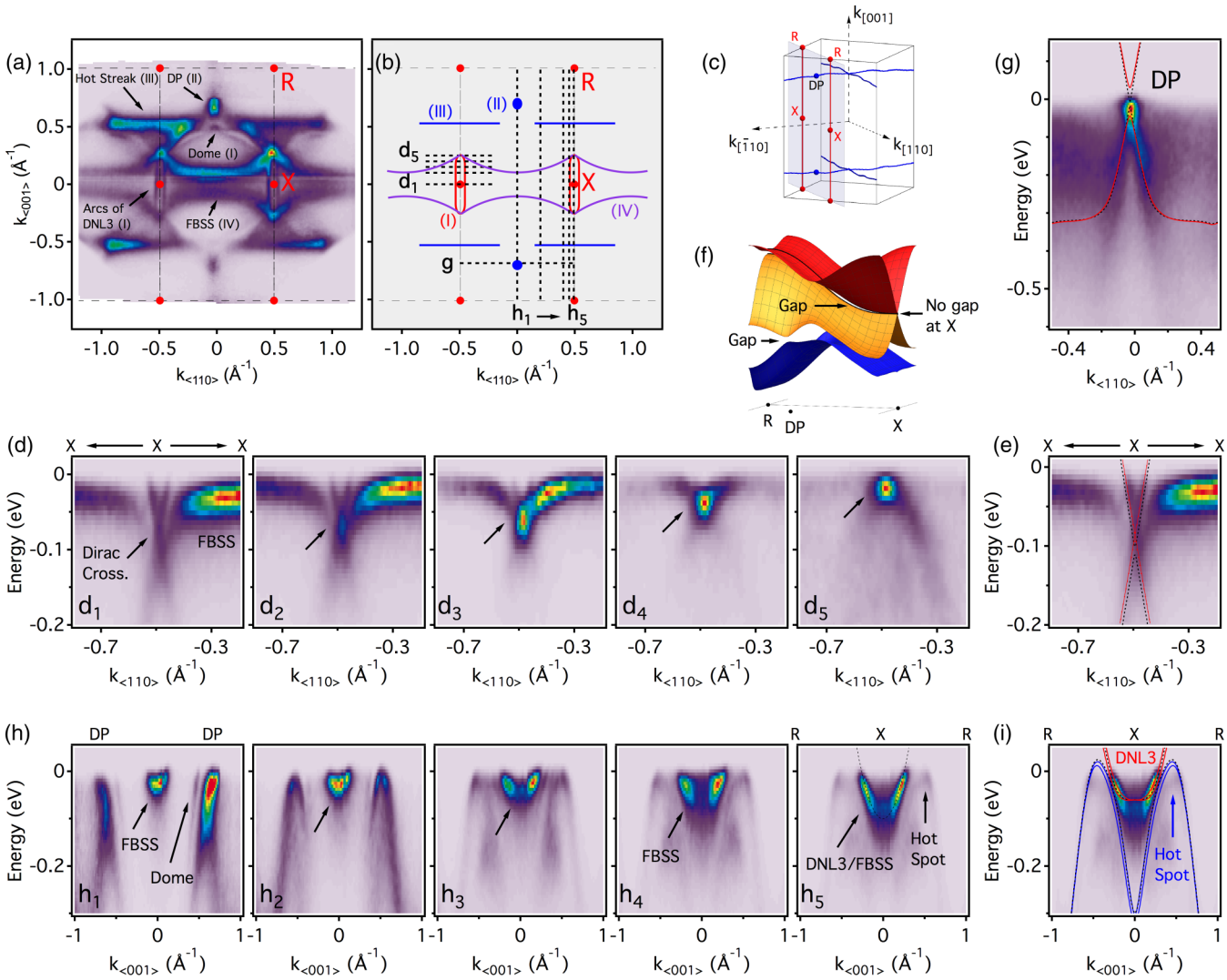

FIG. 2. ARPES in the XR plane. (a) ARPES Fermi surface measured with 69 eV photons. We mark the high-symmetry points (red), the BZ boundaries (black dashed), as well as prominent spectral features (black arrows). (b) Schematic summary of the Fermi surface in (a). Black dotted lines indicate the position of ARPES cuts in panels (d), (g), and (h). (c) The RuO_2 BZ, focusing on the (110) measurement plane containing the X and R high-symmetry points, and its intersection with DNL1 at DP. (d) Energy dispersion along $k_{\langle 110\rangle}$, showing the evolution of the Dirac crossing and the FBSS with $k_{\langle 001\rangle} = 0$ (d_1); $= 0.1$ (d_2); $= 0.15$ (d_3); $= 0.2$ (d_4); $= 0.25$ (d_5). (e) Shifted (see text) DFT (black dotted) and DFT+SOC (red solid) calculations, compared to the ARPES data of (d_1). (f) DFT+SOC band-structure model of RuO_2. In comparison to Fig. 1(b), SOC gaps DNL3 and the DP, but the fourfold band crossing at X is strictly symmetry protected. (g) ARPES close-up of the Dirac crossing at DP, compared to shifted (see text) DFT (black dotted) and DFT+SOC (red solid) calculations. (h) Energy dispersion along $k_{\langle 001\rangle}$ and the evolution of the FBSS with $k_{\langle 110\rangle} = 0$ (h_1); $= 0.2$ (h_2); $= 0.4$ (h_3); $= 0.45$ (h_4); $= 0.495$ (h_5). Along XR (h_5), the FBSS merges with DNL3. (i) Shifted (see text) DFT (black dotted) and DFT+SOC (red solid) calculations, compared to the ARPES data of (h_5). Hot spot bands associated with a Fermi surface instability in Ref. [10] are shown in blue and did not require an energy correction.

but takes a sharp, holelike downward bend to merge with the Dirac crossing at the BZ boundary XR. The ARPES cuts in Fig. 2(h) present the perpendicular dispersion of the FBSS at the BZ center (h_1), and trace its evolution with $k_{\langle 110\rangle}$ (h_{2-4}) as it integrates into the DNL3 in (h_5). Along XR (h_5), DNL3 and the FBSS produce an electronlike parabolic dispersion (black dotted line), with an $\sim$0.1 eV band bottom and $m^* \sim 2.5m_e$ effective mass, well mimicked by the DFT bands (red) in panel (i). The simultaneous electron and hole character, as well as the diverging density of states of the FBSS, are clear hallmarks of a saddle-point van Hove singularity.

Doping evolution of the FBSS. The spanning and anchoring of the FBSS in between adjacent DNL3s, as well as its flat energy dispersion, suggest this state to represent the analog of the drumhead surface state predicted in systems with closed contour DNLs [14,30]. To test its robustness, we deposit potassium at the surface while monitoring the ARPES response *in situ*. An overview of the results is presented in Fig. 3. Panels (a) and (b) show the continuous doping evolution of energy distribution curves (EDCs) at $(k_{\langle 110\rangle}, k_{\langle 001\rangle}) = (0, 0)$ and at the X point, respectively. With increasing electron doping, the FBSS considerably broadens and disperses to ~ -0.43eV

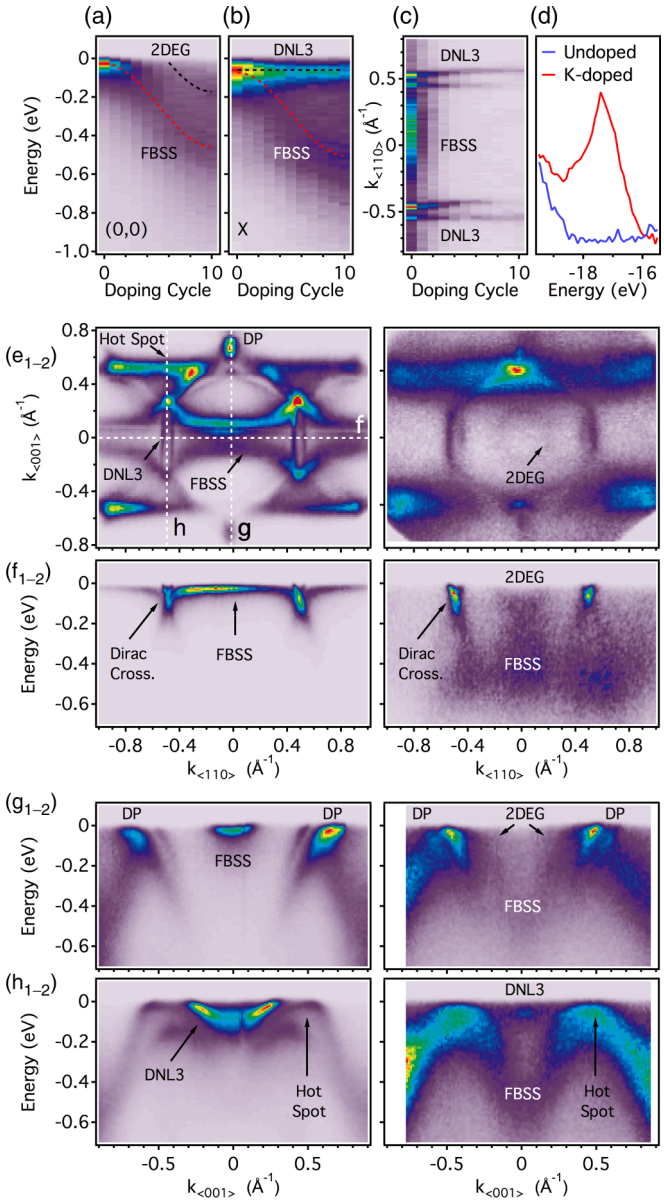

FIG. 3. Doping evolution of the FBSS. (a) EDC at $(k_{\langle 110\rangle}, k_{\langle 001\rangle}) = (0, 0)$, (b) EDC at $(k_{\langle 110\rangle}, k_{\langle 001\rangle}) = (0.495, 0)$ Å^{-1} (X), and (c) MDC at $k_{\langle 001\rangle} = 0$, all measured *in situ* with 69 eV photons as a function of potassium deposition. (d) K 1s core level measurements before (1) and after deposition (2). (e) Fermi surfaces and (f), (h), ARPES band structures along paths indicated in (e$_1$), before (1) and after (2) K deposition.

[red dashed curve in Figs. 3(a) and 3(b)]. The states associated with DNL3 populate only slightly [black dashed curve in Fig. 3(b)], producing the Fermi surface bifurcation in the momentum distribution curve (MDC) of panel (c).

Figure 3(d) shows the K 1s core level peak, and Figs. 3(e)–3(h) show the ARPES data before and after potassium deposition, respectively. With respect to the predeposition Fermi surface in (e$_1$), the postdeposition Fermi surface (e$_2$) reveals overall broader and fuzzier spectral weight. However, whereas the bulk-derived spectral contributions related to DNL3 (I), DP (II), and the hot spot states (III) remain intact, the FBSS disappears and gives way to the faint circular contours of a gas of itinerant surface electrons [two-dimensional electron gas (2DEG)]. The dispersion of the FBSS along $k_{\langle 110\rangle}$ [white dashed line marked "f" in (e$_1$)] before and after deposition is shown in panels (f$_1$) and (f$_2$), respectively. Dropping to higher binding energy, the FBSS produces broad but robust spectral weight at ~ -0.43 eV, while the 2DEG forms a broad parabolic line shape close to E_F. The drop of the FBSS is reproduced in panels (g) along $k_{\langle 001\rangle}$ [marked "g" in (e$_1$)] . The bulk band-derived Dirac crossing at DP, however, stays remarkably intact. In panels (h), the hot spot states gain overall spectral weight with respect to DNL3, seemingly connect to the FBSS, and form a continuous M-shaped-like band contour along $k_{\langle 001\rangle}$ [marked "h" in (e$_1$)].

The sensitive response of the FBSS to surface doping indicates a significant loss of coherence in response to changes in the electrostatic environment. While the potassium-induced surface disorder plays only a minor role, we believe this effect to result from augmented scattering of the FBSS with quasiparticles from the metallic bulk of RuO_2 [30]. Indeed, such scattering is greatly enhanced for van Hove singularities, which enhance the Coulomb interaction and correlation of the surface electrons [32]. Thus, even in the presence of relatively weak perturbations, we may expect exotic symmetry-broken states such as surface magnetism [30], surface superconductivity [31], or graphenelike Landau levels [33], whose experimental exploration we leave for a further study.

Finally, it is intriguing to speculate why the additional DNL3 escaped earlier DFT and symmetry investigations [13]. For one, we note that DFT of pure and Ir-doped RuO_2 consistently misses the correct binding energy of the relevant bands by significant values (at X: 0.56 eV; at DP: 0.15 eV; see also Supplemental Material S5 [27]), and consequently out of reach of the Fermi level. This is a consequence of the oversimplified DFT description of the correlated Ru 4d manifold in RuO_2. Unlike in 5d rutile oxides such as IrO_2 [37,38], the common neglect of correlation effects in 4d transition-metal compounds is hence not entirely justified. Further, SOC is expected to split the DNL3s along XR, an effect that we found to be weak and beyond the resolving power of our experiment. This is in remarkable analogy to the well studied system graphene, a predicted quantum spin-Hall insulator [39], which in view of low SOC presents itself—like RuO_2—as a *de facto* Dirac semimetal [40].

Acknowledgments. We thank Johan Chang, Masafumi Horio, Paul Snijders, and Yan Sun for helpful discussions. S.M. acknowledges support by the Swiss National Science Foundation (Grant No. P300P2-171221). R.J.K. is supported by a fellowship within the Postdoc-Program of the German Academic Exchange Service (DAAD). The Boston University program was supported by the Department of Energy under Grant No. DE-FG02-98ER45680. The theory work was supported by a Consolidator grant of the European Research Council under Project No. 617196, and used resources of IDRIS/GENCI under project gen1393. We thank the computer support team of CPHT. This research further used resources of the Advanced Light Source, which is a DOE Office of Science User Facility under Contract No. DE-AC02-05CH11231.

[1] H. Over, Chem. Rev. **112**, 3356 (2012).

[2] J. Ryan, A. Berry, M. Anderson, J. Long, R. Stroud, V. Cepak, V. Browning, D. Rolison, and C. Merzbacher, Nature (London) **406**, 169 (2000).

[3] Y.-Y. Hu, Z. Liu, K.-W. Nam, O. J. Borkiewicz, J. Cheng, X. Hua, M. T. Dunstan, X. Yu, K. M. Wiaderek, L.-S. Du, K. W. Chapman, P. J. Chupas, X.-Q. Yang, and C. P. Grey, Nat. Mater. **12**, 1130 (2013).

[4] A. Ferris, S. Garbarino, D. Guay, and D. Pech, Adv. Mater. **27**, 6625 (2015).

[5] J. F. Weaver, Chem. Rev. **113**, 4164 (2013).

[6] M. Karamad, H. A. Hansen, J. Rossmeisl, and J. K. Nørskov, ACS Catal. **5**, 4075 (2015).

[7] K. Seki, Catal. Surv. Asia **14**, 168 (2010).

[8] Y. Lee, J. Suntivich, K. J. May, E. E. Perry, and Y. Shao-Horn, J. Phys. Chem. Lett. **3**, 399 (2012).

[9] E. Torun, C. M. Fang, G. A. de Wijs, and R. A. de Groot, J. Phys. Chem. C **117**, 6353 (2013).

[10] T. Berlijn, P. C. Snijders, O. Delaire, H.-D. Zhou, T. A. Maier, H.-B. Cao, S.-X. Chi, M. Matsuda, Y. Wang, M. R. Koehler, P. R. C. Kent, and H. H. Weitering, Phys. Rev. Lett. **118**, 077201 (2017).

[11] F. A. Cotton and J. T. Mague, Inorg. Chem. **5**, 317 (1966).

[12] S. Butler and J. Gillson, Mater. Res. Bull. **6**, 81 (1971).

[13] Y. Sun, Y. Zhang, C.-X. Liu, C. Felser, and B. Yan, Phys. Rev. B **95**, 235104 (2017).

[14] H. Weng, Y. Liang, Q. Xu, R. Yu, Z. Fang, X. Dai, and Y. Kawazoe, Phys. Rev. B **92**, 045108 (2015).

[15] L. M. Schoop, M. N. Ali, C. Straßer, A. Topp, A. Varykhalov, D. Marchenko, V. Duppel, S. S. P. Parkin, B. V. Lotsch, and C. R. Ast, Nat. Commun. **7**, 11696 (2015).

[16] Y. Wu, L.-L. Wang, E. Mun, D. D. Johnson, D. Mou, L. Huang, Y. Lee, S. L. Bud'ko, P. C. Canfield, and A. Kaminski, Nat. Phys. **12**, 667 (2016).

[17] G. Bian, T.-R. Chang, R. Sankar, S.-Y. Xu, H. Zheng, T. Neupert, C.-K. Chiu, S.-M. Huang, G. Chang, I. Belopolski, D. S. Sanchez, M. Neupane, N. Alidoust, C. Liu, B. Wang, C.-C. Lee, H.-T. Jeng, C. Zhang, Z. Yuan, S. Jia, A. Bansil, F. Chou, H. Lin, and M. Z. Hasan, Nat. Commun. **7**, 10556 (2016).

[18] M. Neupane, I. Belopolski, M. M. Hosen, D. S. Sanchez, R. Sankar, M. Szlawska, S.-Y. Xu, K. Dimitri, N. Dhakal, P. Maldonado, P. M. Oppeneer, D. Kaczorowski, F. Chou, M. Z. Hasan, and T. Durakiewicz, Phys. Rev. B **93**, 201104(R) (2016).

[19] S. S. Wang, Y. Liu, Z. M. Yu, X. L. Sheng, and S. A. Yang, Nat. Commun. **8**, 1844 (2017).

[20] R. Yu, Z. Fang, X. Dai, and H. Weng, Front. Phys. **12**, 127202 (2017); Q. Xu, R. Yu, Z. Fang, X. Dai, and H. Weng, Phys. Rev. B **95**, 045136 (2017).

[21] S. A. Ekahana, S.-c. Wu, J. Jiang, K. Okawa, D. Prabhakaran, C.-C. Hwang, S.-K. Mo, T. Sasagawa, C. Felser, B. Yan, Z. Liu, and Y. Chen, New J. Phys. **19**, 065007 (2017).

[22] S.-Y. Yang, H. Yang, E. Derunova, S. S. P. Parkin, B. Yan, and M. N. Ali, Adv. Phys.: X **3**, 1414631 (2018);

[23] R. Lou, P. Guo, M. Li, Q. Wang, Z. Liu, S. Sun, C. Li, X. Wu, Z. Wang, Z. Sun, D. Shen, Y. Huang, K. Liu, Z.-Y. Lu, H. Lei, H. Ding, and S. Wang, npj Quant. Mater. **3**, 43 (2018).

[24] S. M. Young and C. L. Kane, Phys. Rev. Lett. **115**, 126803 (2015).

[25] K. Fujiwara, Y. Fukuma, J. Matsuno, H. Idzuchi, Y. Niimi, Y. Otani, and H. Takagi, Nat. Commun. **4**, 2893 (2013); C. H. Kim, H. S. Kim, H. Jeong, H. Jin, and J. Yu, Phys. Rev. Lett. **108**, 106401 (2012).

[26] A. A. Burkov, M. D. Hook, and L. Balents, Phys. Rev. B **84**, 235126 (2011).

[27] See Supplemental Material at http://link.aps.org/supplemental/10.1103/PhysRevB.98.241101 for sample preparation, experimental methods, as well as complementary ARPES and DFT results.

[28] V. Jovic, R. J. Koch, S. K. Panda, H. Berger, P. Bugnon, A. Magrez, K. E. Smith, S. Biermann, C. Jozwikak, A. Bostwick, E. Rotenberg, and S. Moser (unpublished).

[29] H. Schäfer, G. Schneidereit, and W. Gerhardt, Z. Anorg. Allg. Chem. **319**, 327 (1963).

[30] Y.-H. Chan, C.-K. Chiu, M. Y. Chou, and A. P. Schnyder, Phys. Rev. B **93**, 205132 (2016).

[31] N. B. Kopnin, T. T. Heikkilä, and G. E. Volovik, Phys. Rev. B **83**, 220503 (2011).

[32] Y. Huh, E.-G. Moon, and Y. B. Kim, Phys. Rev. B **93**, 035138 (2016).

[33] J.-W. Rhim and Y. B. Kim, Phys. Rev. B **92**, 045126 (2015).

[34] P. Blaha, K. Schwarz, P. Sorantin, and S. Trickey, Comput. Phys. Commun. **59**, 399 (1990).

[35] A. A. Mostofi, J. R. Yates, G. Pizzi, Y.-S. Lee, I. Souza, D. Vanderbilt, and N. Marzari, Comput. Phys. Commun. **185**, 2309 (2014); A. A. Mostofi, J. R. Yates, Y.-S. Lee, I. Souza, D. Vanderbilt, and N. Marzari, *ibid.* **178**, 685 (2008).

[36] J. Kuneš, R. Arita, P. Wissgott, A. Toschi, H. Ikeda, and K. Held, Comput. Phys. Commun. **181**, 1888 (2010).

[37] J. K. Kawasaki, M. Uchida, H. Paik, D. G. Schlom, and K. M. Shen, Phys. Rev. B **94**, 121104(R) (2016).

[38] P. K. Das, J. Sławińska, I. Vobornik, J. Fujii, A. Regoutz, J. M. Kahk, D. O. Scanlon, B. J. Morgan, C. McGuinness, E. Plekhanov, D. Di Sante, Y.-S. Huang, R.-S. Chen, G. Rossi, S. Picozzi, W. R. Branford, G. Panaccione, and D. J. Payne, Phys. Rev. Mater. **2**, 065001 (2018).

[39] C. L. Kane and E. J. Mele, Phys. Rev. Lett. **95**, 226801 (2005).

[40] A. Bostwick, T. Ohta, T. Seyller, K. Horn, and E. Rotenberg, Nat. Phys. **3**, 36 (2007).